The Distribution of Cloud Horizontal Sizes

ROBERT WOOD
University of Washington, Seattle, Washington

PAUL R. FIELD
Met Office, Exeter, Devon, United Kingdom

(Manuscript received and in final form 13 April 2011)

ABSTRACT

Cloud horizontal size distributions from near-global satellite data, from aircraft, and from a global high-resolution numerical weather prediction model, are presented for the scale range 0.1–8000 km and are shown to be well-represented using a single power-law relationship with an exponent of $\beta = 1.66 \pm 0.04$ from 0.1 to 1500 km or more. At scales longer than 1500 km, there is a statistically significant scale break with fewer very large clouds than expected from the power law. The size distribution is integrated to determine the contribution to cloud cover and visible reflectance from clouds larger than a given size. Globally, clouds with a horizontal dimension of 200 km or more constitute approximately 50% of the cloud cover and 60% of the reflectance, and this result is not sensitive to the minimum size threshold assumed in the integral assuming that the power law can be extrapolated below 100-m scale. The result is also not sensitive to whether the size distribution is determined using cloud segment length or cloud area. This emphasizes the great role played by large cloud sheets in determining the earth's albedo. On the other hand, some 15% of global cloud cover comes from clouds smaller than 10 km, thus emphasizing the broad range of cloud sizes that contribute significantly to the earth's radiation budget. Both of these results stem from the fact that β is slightly less than 2. The data are further divided and geographical and seasonal variations in the cloud size L_{50} for which clouds larger than L_{50} constitute 50% of the cloud cover are determined. The largest clouds ($L_{50} > 300$ km) are found over the midlatitude oceans, particularly in summer, and over the tropical convective regions of the west Pacific and Indian Oceans and the monsoon-influenced landmasses. The smallest clouds ($L_{50} < 100$ km) are found over the trade wind regions of the tropics/subtropics and over arid land areas. Small variations in the exponent β contribute significantly to the variations in L50. Finally, it is shown that a bounded cascade model can faithfully simulate the observed cloud size distributions and use this to examine the effects of limiting sensor resolution (pixel size) and domain size (number of pixels across image). Sensor resolution is not found to strongly impact the cloud size distribution provided the ratio of the domain to pixel size remains greater than ~1000. Thus, previous studies with small domain–pixel size ratios may provide biased information about the true cloud size distribution, and should be interpreted with caution.

1. Introduction

The earth's atmospheric clouds display tremendous variety in form and scale. From fragmentary small cumulus elements to enormous sheets of clouds that swathe much of the midlatitude oceans, clouds are at once both ubiquitous and transitory. The most notable and commonly used attempts to categorize clouds are based on their kilometer-scale (surface based) visual appearance and their altitude, which together form the basis of a classification system, which has survived the technological developments in observation systems of over two centuries. The field of view of a surface-based observer is limited to a few kilometers to at most a couple of tens of kilometers. When spaceborne observing of clouds became routine in the 1960s, we began to greatly expand our appreciation of the horizontal scales of clouds.

Despite the emergence of satellites, the earliest quantitative and focused studies of cloud horizontal sizes used still photography from high-altitude aircraft (see, e.g., Plank 1969). Given that even the field of view from a high-altitude aircraft is itself limited to 100 km at most, it is perhaps not surprising that early studies

---

Corresponding author address: Robert Wood, Department of Atmospheric Sciences, University of Washington, Seattle, WA 98195.
E-mail: robwood@atmos.washington.edu

DOI: 10.1175/2011JCLI4056.1

focused primarily on fair-weather cumulus clouds. Nevertheless, the early scale-classification studies were clear to demonstrate that the smallest observable clouds (in these studies ~50 m) tend to be the most numerous, but that cloud cover is not always dominated by the smallest clouds. The first comprehensive satellite surveys of the horizontal sizes of clouds focused on tropical deep convective clusters rather than fair-weather cumulus clouds since at that time the resolution of the satellite-derived available cloud observations was limited to a few kilometers. Nevertheless, a similar picture emerges from these studies (Machado et al. 1992; Machado and Rossow 1993; Wilcox and Ramanathan 2001; Peters et al. 2009); namely, that the smallest observable cloud clusters are the most numerous, but that there is a significant contribution to cloud cover from clouds of all sizes out to the largest observed horizontal scales (in these studies ~500 km).

With the advent of very high-resolution (~10-m horizontal scale) satellite imagery, fair-weather cumulus clouds have reemerged as the primary cloud type subjected to size distribution classification. Recent studies have confirmed the earliest photographic results showing the numerical dominance of small clouds (Benner and Curry 1998; Zhao and Di Girolamo 2007), and a picture has emerged that the most appropriate quantitative description of the size distribution is a power law. Interestingly, broken stratocumulus clouds also appear to share these characteristics (Welch et al. 1988), with their size distribution assuming power-law behavior with an exponent very close to that for both fair-weather cumulus and large deep convective tropical cloud clusters. The latter is quite remarkable since different processes control these different cloud systems. Furthermore, numerous studies have found that numerous geometric and radiative properties of clouds and rain are fractal in nature (e.g., Lovejoy 1982; Davis et al. 1996; Lovejoy et al. 2001, and references therein), for which the power law is the natural descriptor, or collapse onto simple gamma distributions when normalized (e.g., Field and Shutts 2009).

Cloud size distribution

In general, the number density function $n(x)$ of some measure of cloud geometric property x such that $n(x)\,dx$ is the number of clouds with sizes between x and $x + dx$ per unit sampling interval. In this study x will be used to represent either cloud chord length or projected area. If x is cloud-projected area A, then $n(A)\,dA$ is the number of clouds with areas between A and $A + dA$ per unit area. If x is the cloud chord length L for one-dimensional sampling (e.g., along an aircraft track or using chords from a satellite image), then $n(L)\,dL$ is the number of clouds with horizontal chord lengths between L and $L + dL$ per unit length.

In principle, since clouds can exist on all scales $x \in [0, \infty]$, then $n(x)$ needs to be defined over this entire range, or in practice up to the planetary scale. Since any given set of sensors can only size clouds with a limited size range, in general x is usually measurable over some range $[x_{\min}, x_{\max}]$, where $x_{\min}, x_{\max} \in [0, \infty]$. Then, the fractional cloud *cover* $f_c(x_{\min}, x_{\max})$ of the subset of clouds with sizes between $x_{\min}$ and $x_{\max}$ is

$$f_c(x_{\min}, x_{\max}) = \int_{x_{\min}}^{x_{\max}} x n(x)\,dx \le 1, \tag{1}$$

while the number density $N(x_{\min}, x_{\max})$, which is the *number* of clouds per unit sampling interval of clouds with sizes between $x_{\min}$ and $x_{\max}$ is

$$N(x_{\min}, x_{\max}) = \int_{x_{\min}}^{x_{\max}} n(x)\,dx. \tag{2}$$

If some physical property of the clouds (e.g., solar reflectance) can be defined to be a function $F(x)$ of the cloud size x, then the mean value of this property $\overline{F(x_1, x_2)}$ over all cloudy regions is

$$\overline{F(x_{\min}, x_{\max})} = \int_{x_{\min}}^{x_{\max}} xF(x)n(x)\,dx. \tag{3}$$

As mentioned above, many observational studies have found that $n(x)$ is best represented by a power law or a combination of two power laws. This is the case regardless of whether x represents cloud-projected area A or cloud chord length L, and regardless the cloud scales being considered (e.g., cf. Zhao and Di Girolamo 2007 and Machado and Rossow 1993). For the power-law case, $n(x) = \alpha x^{-\beta}$. Given a power-law density function, the exponent β essentially determines the balance between whether small or large clouds are the dominant contributors to cloud cover. For $\beta = 2$, clouds with logarithmic intervals of size within ($x_{\min}$, $x_{\max}$; e.g., 1–10 units, 10–100 units, etc.) contribute exactly equally to cloud cover. As β becomes progressively smaller than 2, large clouds become increasingly dominant contributors to cloud cover; as β becomes progressively larger than 2, small clouds become increasingly dominant contributors to cloud cover. To see this, we examine the contribution C to cloud cover from clouds larger than some size x within the interval ($x_{\min}$, $x_{\max}$), by setting $n(x) = \alpha x^{-\beta}$, integrating $\int_x^{x_{\max}} xn(x)\,dx$, and dividing by the overall cloud cover f_c from (1) to give

$$C(x) = \frac{1 - (x/x_{\max})^{2-\beta}}{1 - (x_{\min}/x_{\max})^{2-\beta}}\,. \tag{4}$$

We will examine the case where $x_{\min}/x_{\max} \ll 1$ (i.e., where the power law extends over several orders of

(a) cover contribution from clouds larger than x/x_{max}

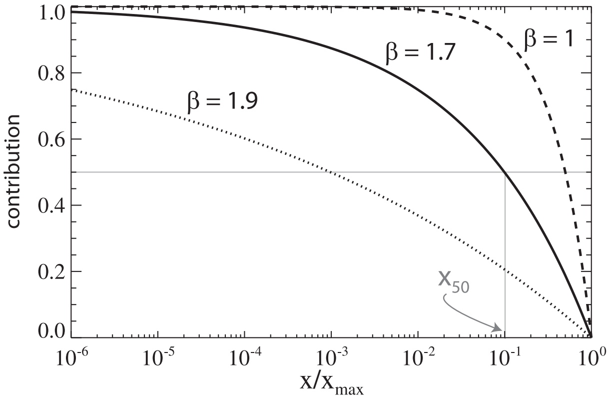

(b) cover contribution from clouds larger than x/x_{min}

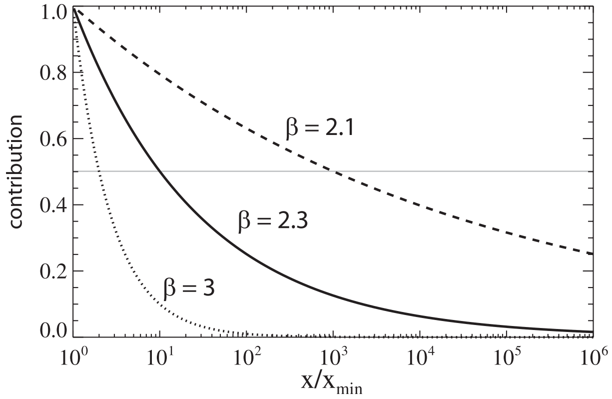

FIG. 1. Contribution to cloud cover from (a) clouds larger than x/x_{max} for the case where $\beta < 2$, and (b) clouds larger than x/x_{max} for the case where $\beta > 2$. The 50% line is included for reference and x_{50} is a characteristic cloud size such that clouds larger than x_{50} contribute 50% of the cloud cover.

magnitude, as is shown to be the case below). Then, we need to consider two cases, $\beta < 2$ and $\beta > 2$. For these cases, we have

$$\lim_{x_{\text{min}}/x_{\text{max}} \to 0} C(x) = 1 - (x/x_{\text{max}})^{2-\beta} \quad (\beta < 2) \qquad (5)$$

$$= (x_{\text{min}}/x)^{\beta-2} \quad (\beta > 2). \qquad (6)$$

These are shown graphically in Fig. 1 for various values of β. Here, we introduce a characteristic cloud size x_{50} such that clouds larger than x_{50} contribute 50% of the cloud cover. The essential behavior is that for $\beta < 2$, x_{50} is determined by the upper bound on x (i.e., the largest clouds in the size distribution), while for $\beta > 2$, x_{50} is determined by the smallest clouds. While this is not a new point (see, e.g., Neggers et al. 2003), Fig. 1 is a useful way of quantifying just how important large and small clouds are. For example, we can see from Fig. 1 that when β assumes values far from 2 (e.g., 1 or 3), the value of x_{50} is very close to the limit sizes (i.e., x_{max} or x_{min}). In this case, only a small subset of the range (x_{min}, x_{max}) contributes significantly to cloud cover.

In contrast, when β is within a few tenths of 2 (e.g., 1.7 or 2.3), we can see from the less steeply curved nature of the relationships in Fig. 1 that a large range of cloud sizes actually contribute significantly to the cloud cover. For example, with $\beta = 1.7$, let us assume that x_{max} is the planetary scale (of order 1000 km for simplicity). In this case, the contribution to cloud cover from clouds $100 < x < 1000$ km is 50%, the contribution from clouds $10 < x < 100$ km is 25%, the contribution from clouds $1 < x < 10$ km is 13%, and even clouds $0.1 < x < 1$ km contribute 6% to overall cloud cover. This implies that clouds over a huge range of scales still contribute significantly to cloud cover, even though (since $\beta < 2$) the largest clouds dominate.

In this study we use satellite and aircraft data, together with a global forecast model, spanning almost five orders of cloud horizontal scale (0.1–8000 km) to explore the cloud size distribution globally, seasonally, and regionally. We also explore the observed distributions using a simple fractal model. Section 2 describes the data and methodology. Section 3 provides the bulk of the observational results, while section 4 presents the fractal model and explores some of its behavior. Discussion and conclusions are presented in section 5.

2. Data and methods

In this paper we construct cloud chord length and cloud-projected area distributions using data from the Moderate Resolution Imaging Spectroradiometer (MODIS) on the National Aeronautics and Space Administration (NASA) *Terra* satellite, and cloud chord length distributions from observational data collected using research aircraft and global model data from the Met Office Unified Model.

a. MODIS data

MODIS is a 36-band scanning spectroradiometer on board the *Terra* satellite. *Terra* is sun synchronous with equatorial crossing times of 1030 and 2230 LT, but in this study we use only daytime data since the addition of reflected solar radiation permits a more robust cloud detection. Data have an along-track footprint size of ~1 km, and a cross-track footprint size that varies from ~1 km at nadir to ~5 km at the largest satellite zenith angles used (approximately 60°). We use data only for satellite zenith angles <45° (i.e., the central 1030 pixels, or 1280 km, of the swath), which eliminates the very broad pixels at edge of the swath that are more difficult to cloud classify, but retains a large coverage. We use the cloud mask product (Ackerman et al. 1998) reported in the MOD06 level 2 (collection 5) cloud product (Platnick et al. 2003). We define a pixel as cloudy only if the unobstructed field-of-view (FOV) confidence flag is zero. Uncertain pixels are determined to be clear for the purposes of this study, but we find that our results are not highly sensitive to this assumption since the number of uncertain pixels is generally quite small. Data over both land and ocean are used.

In addition to determining cloud horizontal sizes with MODIS, we also use MOD02 level 1B (collection 5) visible reflectance estimates at 1-km nadir resolution (i.e., pixel matched with the 1-km cloud mask data described above) to estimate, for each identified–sized cloud, its mean visible reflectance at a wavelength of 0.65 μm (MODIS channel 1). This reflectance is an imperfect, but useful assessment of the broadband cloud albedo.

1) CHORD LENGTH DISTRIBUTIONS

To determine cloud sizes, we use two different methods. For the cloud chord length distribution (which constitutes the majority of the results in this study) we use the along-track direction as our chord direction. We use either single MODIS data granules (each with 1030 pixels cross track and 2030 pixels along track), or up to four sequential granules joined together in the along-track direction. (We vary the number of granules used to examine the impact of their limited length on the derived size distributions.) For each granule or granule chain this gives 1030 strips that are either 2030 pixels ($\approx$2030 km) long in the case of the single granule, or up to 8120 pixels ($\approx$8120 km) in length (for the 4 granule case). We refer to the length of the strip used as the sample length D. For each of these strips, we classify each pixel as either cloudy or clear using the cloud mask. In some cases, the cloud mask flag was not determined (e.g., due to poor data quality). If any pixels in the strip are undetermined we do not process the strip. Otherwise, we use an algorithm to determine the cloud chord lengths L for all the clouds along each strip. The cloud chord length distribution $n(L)$ is then derived by adding up the total number of clouds N_i with lengths between the (approximately logarithmic) bin boundaries L_{i-} and L_{i+}, and then dividing by the bin width $L_{i+} - L_{i-}$ and the total transect length D_{tot} sampled for all strips {i.e., $n(L) = N_i/[D_{\text{tot}}(L_{i+} - L_{i-})]$}.

If the first or last pixel in the strip contains cloud then we cannot determine the size of the cloud containing this pixel (since it may extend beyond the granule). These clouds are then ignored, but the total transect length sampled is still counted in creating the distribution $n(L)$. This introduces a size-dependent sampling bias into the derived chord length distributions because large clouds (clouds with many pixels) will be undersampled. For a cloud with chord length L (measured in pixels) and a sample length D, the start of the cloud (the first cloudy pixel along the strip) can only occur somewhere in the range pixel 2 to pixel $D - L$ if it is to be counted (otherwise the cloud will extend beyond the end of the strip and will not be counted). This reduces the effective sample length for clouds of length L to $D - L - 1$ pixels compared with D pixels for a very small cloud. The eventual size distributions generated by aggregating many strips are then corrected to account for this by correcting the measured chord length distribution $\tilde{n}(L)$ to give the corrected chord length distribution $n(L)$ using the following:

$$n(L) = \frac{D\tilde{n}(L)}{D - L - 1}. \tag{7}$$

This correction is essentially identical to the corrections made to cloud particle size distributions from optical array probes (see, e.g., section 4a in Knollenberg 1970).

Cloud chord length size distributions $n(L)$ are then estimated using the results from many strips and an arbitrary selection of granules, as described below. We also compare cloud chord length distributions taken in the across-track rather than the along-track direction. We found that these were essentially indistinguishable from those in the along-track direction, other than they are necessarily truncated at 1280 km (1030 pixels), since this is the maximum chord length permissible in the across-track direction.

2) CLOUD AREA DISTRIBUTIONS

We also derive cloud-projected area distributions in this study using the same MODIS data used for the chord length distributions. We use the same central portion of the MODIS data granule, but now identify contiguous cloudy areas with a recursive algorithm that finds all the clouds in the granule. Here, pixels adjacent in the diagonal direction are considered to be contiguous. The decision to include diagonals as contiguous primarily affects the smallest area categories and was not found to have a significant effect on the distributions overall.

As with cloud chord length distributions, clouds touching the edge of the granule are omitted from the analysis. Corrections to the size distribution for the reduced effective sample area for large clouds are more difficult in two dimensions since cloud shapes are fractal (Lovejoy 1982), but we can make an attempt to correct using the assumption that cloud-projected areas are square shaped. The corrected area distribution $n(A)$ is derived from the measured one $\tilde{n}(A)$ using the following:

TABLE 1. Power-law exponents for cloud chord length distributions from aircraft data and from MODIS for different data subsets and for different assumptions regarding cloud classification. The last two lines give the exponents for the ensemble data from all cases shown in Fig. 2.

Source	Clouds	Region	Flights	Altitude	Period	Instrument	Threshold	β
Aircraft	Frontal	British Isles	A639, 643, and 656	1–8 km	Nov 1998–Mar 1999	2D-C	5 L^{-1}	1.77 ±0.06
Aircraft	Cirrus	″	A800, 801, and 802	6–10 km	Oct 2000	2D-C	1 L^{-1}	1.63 ±0.06
Aircraft	Cirrus	″	″	″	″	2D-C	5 L^{-1}	1.62 ±0.05
Aircraft	Cirrus	″	″	″	″	2D-C	20 L^{-1}	1.76 ±0.09
Aircraft	Cirrus	″	″	″	″	2D-C	100 L^{-1}	1.71 ±0.07
Aircraft	Cirrus	″	″	″	″	FSSP	0.1 cm^{-3}	1.51 ±0.08
Aircraft	Sc	NE Pacific	H801–H813	0.5–1.5 km	Jul 1997	JW	0.03 g kg^{-1}	1.66 ±0.06
Aircraft	Sc/Cu	NE Atlantic	A203–A215	0.5–2 km	Jun 1992	JW	0.03 g kg^{-1}	1.69 ±0.05
Aircraft	All	All above	All above	0.5–10 km	All above	All	0.03 g kg^{-1}/5 L^{-1}	1.61 ±0.06
Satellite	All	Near global	—	All	2008	MODIS	Cloud mask	1.67 ±0.06

$$n(A) = \frac{WD\tilde{n}(A)}{(W - \sqrt{A} - 1)(D - \sqrt{A} - 1)}, \qquad (8)$$

where W is the (across track) width of the granule, and D is its (along track) length. For the MODIS granule, this becomes a significant correction $[n(A)/\tilde{n}(A) \sim 2]$ where the projected area exceeds $\sim 10^5$ pixels (km^2). Only granules for which the entire granule is sunlit and for which the cloud mask flag is determined on >99% of pixels are used in the analysis.

3) MODIS DATA SELECTION

In this study, we analyze a total of two full years of near-global MODIS data for 2008 and 2009. On each day, all suitable daytime granules are used, making a total of more than 10^4 granules ($\sim 2 \times 10^{11}$ pixels in total). We examine properties of the entire dataset (annual) and we perform a breakdown into geographic regions and four seasons [December–February (DJF), March–May (MAM), June–August (JJA), September–November (SON)].

b. Aircraft data

Aircraft data used in this study are taken from 31 flights flown during various field campaigns of the Met Office C-130 research aircraft. The flights sampled a range of clouds ranging from marine stratocumulus [First International Satellite Cloud Climatology Project (ISCCP) Regional Experiment (FIRE) campaign], stratocumulus-to-cumulus transition [Atlantic Stratocumulus Transition Experiment (ASTEX) campaign], cirrus, and frontal clouds (see Table 1). A total of 355 aircraft legs of length 40–80 km are used. Details of the FIRE and ASTEX flights used are given in Wood and Field (2000) and references therein, while Table 1 lists the cirrus and frontal cloud flights.

Cloud chord length distributions are derived from the aircraft data using the method described in Rodts et al. (2003). Samples at 1 Hz (≈100-m horizontal distance) are classified as either clear or cloudy using thresholds applied to data from cloud-detecting probes. For the exclusively liquid clouds, we use a hotwire probe [Johnson–Williams, see Wood and Field (2000) for details] to determine the cloud liquid water content, and apply a threshold of 0.03 g kg^{-1} to indicate cloud. This threshold is chosen to be as close to zero as possible without producing false alarms due to the instrument noise floor. Alternatively, the use of cloud droplet concentration measured using a Forward Scattering Spectrometer Probe (FSSP) with a 5-cm^{-3} threshold produced similar results in liquid clouds. For the cloud containing predominantly ice (or mixed phase) we use the 2D-C optical array probe that counts and sizes particles in the size range (100–800 μm). We apply a threshold such that the total concentration of particles has to exceed 5 L^{-1}, but examine the sensitivity to this choice below.

Aircraft cloud chord length distributions were produced in exactly the same way as those for the satellite chord lengths, including a sampling correction like that in Eq. (5). Since the aircraft dataset size (a total of $\sim 2 \times 10^5$ 100-m samples) is vastly smaller than the satellite dataset ($\sim 2 \times 10^{11}$ samples), all the aircraft data are grouped together to produce a single cloud chord length distribution. The fact that our observed cloud size distributions are not particularly sensitive to the cloud type (Table 1) provides some justification for doing this.

SENSITIVITY TO INSTRUMENTS/THRESHOLDS

We explore the effects on the cloud chord length distributions of using different cloud detection threshold values and different probes, but all were found to result in distributions with very similar scaling properties. Table 1 lists exponents for power-law fits to the cloud

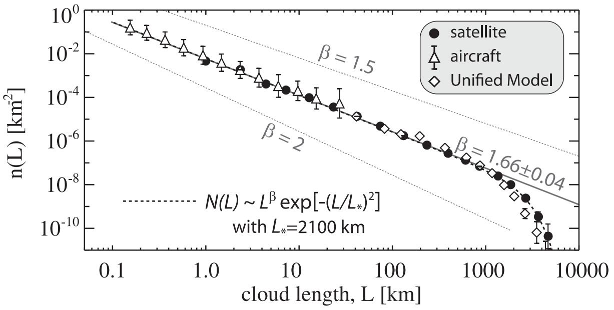

FIG. 2. Aggregate cloud chord length L distribution $n(L)$ produced from all MODIS satellite (filled circles), aircraft (open triangles), and UM (diamonds) data used in this study. The MODIS along-track sample length was 8120 pixels, which was obtained using 4 granules. Error bars indicate the approximate 95% confidence interval. Small multiplicative factors have been applied to minimize the differences between the distributions from the three sources in the regions of overlap. The middle sloping line shows the best-fit regression for the observations estimated using the aircraft and satellite data ($\beta = 1.66 \pm 0.04$), while the two other lines have exponents $\beta = 1.5$ and 2. The darker curve shows a power-law distribution with an exponential drop-off for $L > L_*$, where L_* is estimated from the satellite data to be ~2100 km.

chord length size distribution derived using different ice crystal concentration thresholds for the cirrus clouds, including the effect of changing the instrument to an FSSP for the detection of ice. For all these sensitivity tests in the cirrus case, we found that the exponent β ranges from 1.51 to 1.76 (see Table 1), which is a relatively small variation. In addition, the sensitivity is not monotonic with changing threshold. We can conclude therefore, that the scaling exponents we derive from aircraft data are not highly sensitive to the choice of cloud-detection methodology.

c. Global model data

In addition to observed cloud size distributions, we also analyze data from the Met Office Unified Model (UM). The UM is a nonhydrostatic model (Cullen et al. 1997; Davies et al. 2005). The model includes parameterizations to represent the boundary layer (Lock et al. 2000) cloud cover and condensate (Smith 1990), mixed phase cloud microphysics (Wilson and Ballard 1999), land surface Essery et al. (2003), and convection (Gregory and Rowntree 1990). We use the global operational UM run at 40-km horizontal resolution. Cloud size distributions are produced using the cloud-projected chord length approach in the zonal and meridional directions. To classify as cloudy, columns must contain at least one model grid box with a diagnosed cloud fraction in excess of 99%. No correction is made for sampling since the domain is periodic in the zonal direction and 20 000 km in the meridional direction. A total of 120 days of model output data spaced 3 days apart from 2008 are used in this analysis. For each day we use the 6-h forecast from the run initialized at 1200 UTC.

3. Observational results

a. Observed near-global size distributions

We group the clouds from 2 yr of MODIS data together and produce a single cloud chord length distribution (using 4 granules together to give the maximum sample length of ~8000 km). This, together with the ensemble aircraft and UM chord length distributions, is shown in Fig. 2. Logarithmically spaced bins are used to display the distributions. Sampling errors are estimated as the Poisson counting errors (i.e., $2\sqrt{N}$, where N is the number of independent clouds in each size category) to give errors at approximately the 95% confidence level. For aircraft data we assume all sampled cloud chords to be independent. For the MODIS data and the UM model output each cloud chord is not necessarily independent of adjacent ones since cloud-projected areas can be sampled twice in different chords across the swath/domain. For these, we estimate the approximate number of independent clouds by assuming that clouds with size L (in pixels or model grid boxes) are sampled in L consecutive chords across the swath. In other words, the clouds are assumed to have aspect ratios that are approximately unity. Thus, we divide the actual number of cloud chords by their pixel size to arrive at an approximate number of independent clouds sampled. This probably results in a slight underestimate of the number of independent clouds sampled, and therefore a useful upper bound on the sampling error.

Since from Eq. (1) the integral of $Ln(L)$ over L is equal to the cloud fraction, and since the size distributions from the three sources span different size ranges, we have normalized the distributions so that they would have the same cloud fraction when the size distributions are extrapolated over the same chord size range (L from 0.1 to 1000 km). Small scale-independent multiplicative factors are applied to the distributions to do this.

What is remarkable from Fig. 2 is that the observations indicate that the cloud size distribution $n(L)$ follows a single power-law relationship that spans over four orders of magnitude of cloud horizontal scales, for $0.1 < L < 1000$ km. The exponents for the aircraft data ($\beta = 1.61 \pm 0.06$) and the MODIS data ($\beta = 1.67 \pm 0.06$) taken separately are given in Table 1. The exponent of the overall power law is estimated as $\beta = 1.66 \pm 0.04$ with the error estimated at the 95% level. The UM data show a distribution consistent with this same scaling for

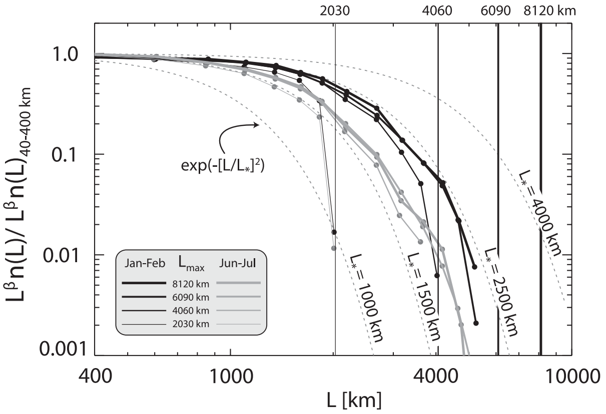

FIG. 3. Cloud chord length L distributions plotted as $L^{1.66}n(L)$ normalized by the mean value of $L^{1.66}n(L)$ for $40 < L < 400$ km to emphasize the departure (scale break) from the $\beta = 1.66$ power-law scaling at large scales. The distributions are produced from all MODIS satellite data for January–February (black) and June–July (gray), with the line thickness indicating the number of MODIS granules conjoined prior to determining the cloud sizes. The gray dashed lines show $y = \exp[-(L/L_*^2)]$ for $L_* = 1000$, 1500, 2500, and 4000 km. The JFM and JJA distributions are quite well represented with $L_* = 2400$ km and $L_* = 1750$ km, respectively.

$40 < L < 1000$ km. For L larger than approximately 1500–2000 km, both the satellite data and the UM indicate a statistically robust scale break, which can be represented mathematically using the size distribution

$$n(L) \sim L^{-\beta} \exp[-(L/L_*)^2], \tag{9}$$

where L_* determines the location of the scale break. From the near-global MODIS size distributions, L_* is estimated to be approximately 2000 km (Fig. 2), and slightly smaller for the UM (Fig. 1). Investigation with smaller numbers of conjoined granules (from 1 to 4) indicates that the value of L_* becomes insensitive to the sample length D for 2 granules ($D \sim 4000$ km) or more (Fig. 3). This suggests that the scale break at $L \sim 2000$ km is a physical entity and not a sampling artifact of having too small a domain. That the UM data also display a similar scale break gives further weight to this conclusion. We will discuss the significance and possible causes of the scale break further in section 3d.

As a further test for possible sampling artifacts, we conducted a suite of Monte Carlo simulations in which we choose clouds with chord lengths from an assumed power-law distribution that extends to the planetary scale (40 000 km). We sample these randomly and place them sequentially on a long (10^6 pixels km^{-1}) one-dimensional array. We assume that the gaps between clouds also follows a power-law distribution with the same exponent but with a constant such that the overall cloud cover is 65%, which is consistent with observations. We then chop up the long arrays to the desired sampling length (which we varied from 2000 to 8000 pixels to simulate the effect of 1–4 MODIS granules) and reconstruct the cloud chord size distributions from many of these subsamples. We found that sampling related deviations from the assumed power law are only a significant problem for clouds with sizes of >75% of the sample length. Thus, if the true description of the cloud size distribution is a single power law extending to the planetary scale, we should not see deviations from the power law at $L \sim 2000$ km when we use 2 ($D \sim 4000$ km) or 4 ($D \sim 8000$ km) conjoined MODIS granules. Since we do indeed see these deviations, this provides additional weight that sampling artifacts are not the cause of the observed scale break.

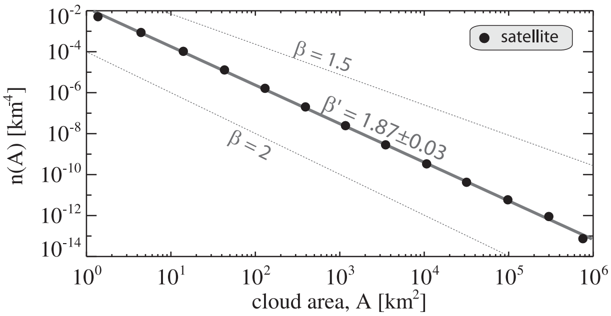

FIG. 4. Aggregate cloud area A distribution $n(A)$ produced from all MODIS satellite data (filled circles). Error bars indicating the approximate 95% confidence interval are too small to show up and are less than 6% even for the larger A bins. The thick line shows the best-fit regression line for the observations estimated using the aircraft and satellite data ($\beta = 1.80 \pm 0.03$), while the thinner dotted lines have exponents $\beta = 1.5$ and 2.

CLOUD-PROJECTED AREA DISTRIBUTION

A cloud-projected area size distribution for the entire MODIS dataset (Fig. 4) can also be explained with a single power law $\beta' = 1.87 \pm 0.03$, spanning six orders of magnitude of cloud area (i.e., for $1 < A < 10^6$ km^2). There is some evidence for a scale break at the larger sizes, but since the sampling corrections at large sizes are more ambiguous we are not as certain about this result as we are for the cloud chord length distributions. Since the power-law scaling appears to reach to $A \sim 10^6$ km^2, this is consistent with the scaling of the chord length distributions (i.e., scaling out to horizontal dimensions of order 1000 km). In this sense there is consistency between the projected area view and the chord length view. Both $n(A)$ and $n(L)$ have values of $\beta < 2$ consistent with large clouds dominating cloud cover, and both have β sufficiently close to 2 that it is clear that *clouds spanning a wide range of horizontal scales contribute*

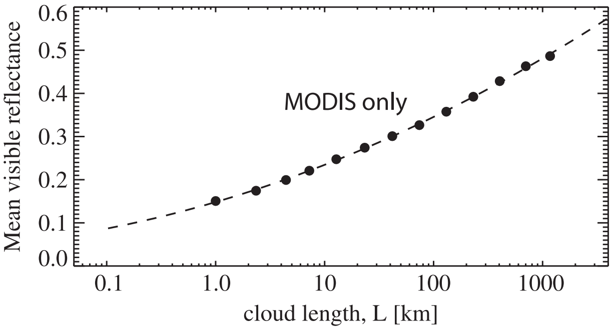

FIG. 5. Mean visible reflectance of clouds as a function of chord length L. The dashed line is a fitted curve with the form $\overline{R_{\mathrm{vis}}} = 0.148 + 0.074\log_{10}L + 0.012(\log_{10}L)^2$.

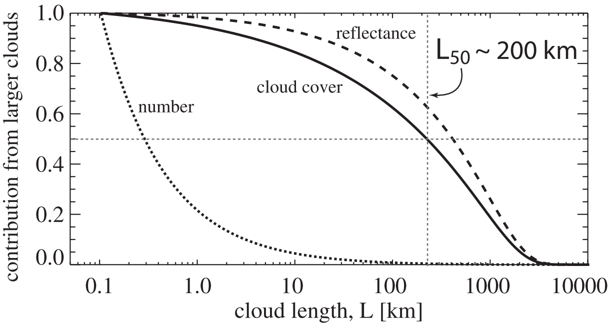

FIG. 6. Contribution to global cloud cover (solid line), number (dotted line), and visible reflectance (dashed line) from clouds with chord lengths greater than L, assuming that the minimum cloud chord length is 0.1 km.

significantly to cloud cover globally. We examine these contributions more specifically below.

b. Contribution of different sized clouds to cloud cover and reflectance

As we discussed in the introduction, we can use the size distributions and Eqs. (1) and (2) to determine the contribution of clouds larger than a given size to the cloud cover and total number density [and, through Eq. (3) any other variable that scales with the cloud size].

Since one of the primary roles that clouds play is to determine the earth's albedo, we also choose to examine the contribution of clouds of different sizes to the visible reflectance. To do this we use the visible reflectance data for each identified cloud and bin this by the cloud chord length L to obtain a relationship between the mean reflectance $\overline{R_{\mathrm{vis}}}$ and L. This is shown in Fig. 5, which demonstrates that clouds with larger horizontal scale tend to be more reflective. Some part of this behavior may be attributed to there being some tendency for clouds to be larger at higher latitudes (see section 3c below). The solar zenith angle tends increases with latitude, and since the visible reflectance of a cloud tends to increase with solar zenith angle (see e.g., King and Harshvardhan 1986), this would lead to higher reflectance for larger clouds simply by virtue of their preference for higher latitudes. However, since the latitudinal dependence of cloud size is not particularly strong, we attribute much of the reflectance increase with L to be indicative of cloud optical thickness increases that vary quasi-linearly with the logarithm of the cloud horizontal scale. In any case, an excellent fit to the data in Fig. 5 is

$$\overline{R_{\mathrm{vis}}} = 0.148 + 0.074\log_{10}L + 0.012(\log_{10}L)^2. \qquad (10)$$

We use the fit in Eq. (10) in conjunction with the fit in (9) to the satellite- and aircraft-observed chord length distribution to determine the contribution of clouds of different sizes to the visible reflectance. Of course, since reflectance data were only available over the chord size range 1–1000 km, we need to extrapolate this to the smallest size for which $n(L)$ is known (0.1 km). We do this by extrapolating Eq. (10) to $L = 0.1$ km, where $R_{\mathrm{vis}} = 0.09$. The results are shown in Fig. 6. Since the observed exponent β is essentially the same as that used in the theoretical example discussed above and shown in Fig. 1, the contribution to the cloud area curve has a similar form to Eq. (5). Differences arise at the large end of the distribution where the fitted form in (9) is truncated by the exponential scale break. Nevertheless, the results in Fig. 6 demonstrate that approximately 50% of the cloud cover globally can be attributed to clouds with horizontal scales L greater than 200 km (i.e., $L_{50} \sim 200$ km). For the pure exponential with an abruptly truncated upper limit at $L = L_{\max}$ [i.e., Eq. (5)], and $\beta = 1.7$, we see that $x_{50}/x_{\max} \approx 0.1$ (Fig. 1a). This is consistent with our finding that $L_{50}/L_* \sim 200/2000 = 0.1$. This means that the steep reduction in $n(L)$ at $L > L_*$ to values below that expected for the power-law scaling is more important than the precise mathematical form to describe the observed scale break.

Nevertheless, the existence and location of the scale break (see section 3d) does limit significantly the value of L_{50}. The value of L_{50} increases quasi-linearly with L_*. The planetary scale (~40 000 km), which has been suggested in some studies (e.g., Lovejoy et al. 2001; Lovejoy and Schertzer 2006) to be the appropriate value for $L_{\max}$ is an order of magnitude larger than L_*, so the location of this scale break is actually very important in determining which cloud sizes contribute most to the overall cloud cover.

Since visible reflectance tends to increase with L (Fig. 5), we find that the cloud chord length L that contributes 50% to the visible reflectance is somewhat greater than L_{50}, being closer to $L \sim 400$ km (Fig. 6). These results reinforce

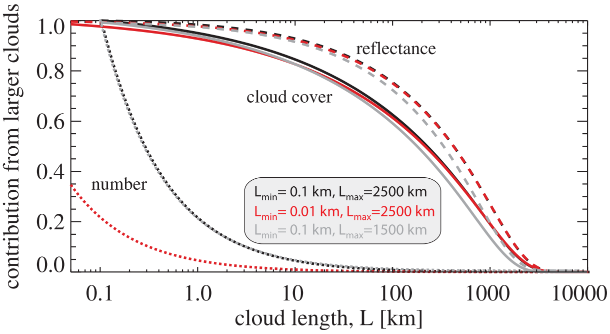

FIG. 7. Sensitivity to the minimum cloud chord size ($L_{\min}$) of the contributions to global cloud cover (solid line), number (dotted line), and visible reflectance (dashed line) from clouds with chord lengths greater than L. The black curves are as shown in Fig. 6 [i.e., $L_{\min} = 0.1$ km ($L_* = 2400$ km)], and the red curves are for $L_{\min} = 0.01$ km ($L_* = 2400$ km). The gray curves show the impact of changing the location of the scale break (i.e., L_*) with $L_{\min} = 0.1$ km and $L_* = 1500$ km.

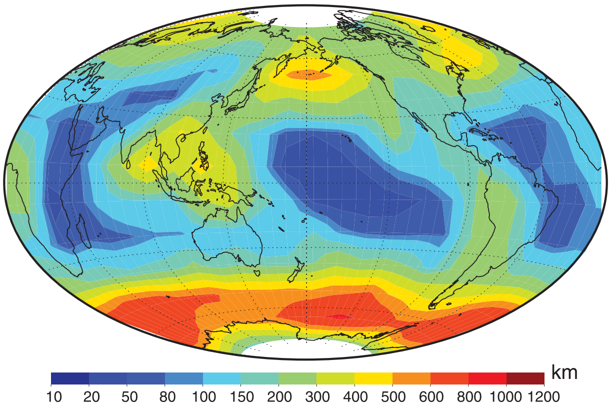

FIG. 8. Map of L_{50} (i.e., the cloud size for which 50% of cloud cover comes from larger clouds) for all 2 yr of MODIS data. To create the map, we aggregate the MODIS-derived size distributions into approximately 20° × 20° regions. For each region we use a power-law fit to size distribution $1 < L < 100$ km and extrapolate the size distribution down to $L = 0.01$ km to include the potential effects of small clouds assuming that the power law continues to these sizes. For regions where $L_{50} > 100$ km the extrapolation decreases L_{50} from its estimation with MODIS data alone by 30% or less, but the extrapolation can decrease L_{50} by a factor of 5 for the few regions with the smallest clouds ($L_{50} < 10$ km).

previous findings emphasizing the importance of the large cloud sheets for the earth's radiation budget. They also demonstrate that a large range of cloud sizes contributes significantly. For the ''near global'' distribution shown in Fig. 2, the approximate contributions to cloud cover from decadal intervals are as follows: $L < 1$ km (5%), $1 < L < 10$ km (10%), $10 < L < 100$ km (20%), $100 < L < 1000$ km (40%), and $L > 1000$ km (20%).

On the other hand, the cloud number density is always dominated by the smallest clouds, as expected. Figure 7 shows that there is little sensitivity to the assumed minimum cloud size $L_{\min}$ in terms of cloud cover and reflectance, but a huge sensitivity in terms of the cloud number density. When the size distribution is extended down from 100 to 10 m, the chord length for which 50% of clouds are larger reduces from 300 to 30 m. However, the contribution of these smallest clouds to the global cloud cover and reflectance is very small. Certainly one can find cases in which very small clouds dominate the cloud cover (e.g., Plank 1969; Koren et al. 2008), but these cases are certainly not globally representative. Figure 7 also demonstrates that the variability in the precise location of the scale break (i.e., the values of L_*) has a relatively small effect on the contribution to cloud sizes. Decreasing L_* from 2400 to 1500 km, encompassing the range in L_* for the JFM and JJA global distributions (Fig. 3) decreases the characteristic chord length L_{50} by approximately 25% (see Fig. 7).

c. *Geographic and seasonal variation of cloud size*

We examine the geographic variability in the characteristic chord length L_{50} in Fig. 8 (annual data) and Fig. 9 (seasonal breakdown). To improve the localization, the geographical variability analysis uses two conjoined MODIS granules rather than four, since we have shown that the size distributions converge for two or more granules (section 3a). There is marked geographical variability in L_{50}, which can range from a few kilometers to >500 km from region to region. The key features are that the largest clouds tend to be found over the midlatitude oceans, particularly in the summer months, and over regions–seasons with strong tropical convection (e.g., the Southeast Asian monsoon during summer and the tropical west Pacific during winter). In these regions L_{50} is several hundred kilometers or greater. Large clouds are also common over the stratocumulus regions of the eastern subtropical oceans. In contrast, low values of L_{50} are associated with oceanic trade wind cumulus regions, especially in the central Pacific, and continental regions during dry seasons.

Boundary layer structure is clearly important for controlling L_{50} in regions where low clouds dominate cloud cover. Increasing MBL depth is associated with smaller L_{50}. Over subtropical oceans, MBL depth is inversely related to low cloud fraction (Wood and Hartmann 2006). As the MBL deepens, typically due to increased surface fluxes a well-mixed boundary layer that can support extensive saturated conditions near its top can no longer be maintained, and the MBL decouples (e.g., Albrecht et al. 1995; Bretherton and Wyant 1997; Wood and Bretherton 2004). This increases the vertical stratification in the MBL and increasing horizontal variability with the result being cloud breakup.

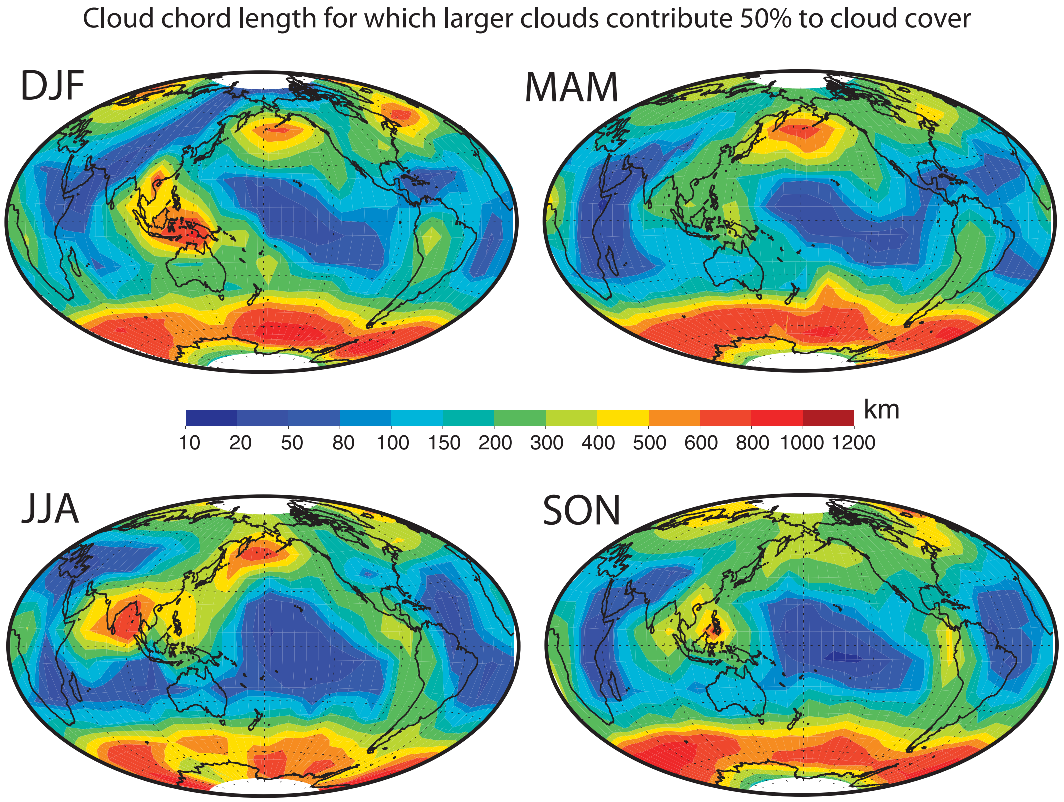

FIG. 9. As in Fig. 8, but broken down by season with maps for (top left) JFM, (top right) MAM, (bottom left) JJA, and (bottom right) SON.

Not surprisingly, the results indicate that high values of L_{50} are generally associated with regions of extensive mean cloud cover. The midlatitude oceans, particularly during summer months, are some of the cloudiest regions on the earth (see, e.g., Klein and Hartmann 1993). But the mean cloud cover $\overline{f}_c$ does not completely determine the magnitude of L_{50} as Fig. 10 indicates. What is particularly interesting is that the correlation between L_{50} and $\overline{f}_c$ is markedly stronger over the ocean than it is over the land. Also, over the ocean, L_{50} is larger for the same $\overline{f}_c$ during the summer compared with the winter. Further exploration indicates that the larger L_{50} values during the summer are typically associated with the large sheets of summertime stratus and fog that are known to dominate the midlatitude oceans (Klein and Hartmann 1993). Over land, there is no clear difference between the ratio of L_{50} to $\overline{f}_c$ for winter and summer. It is also very interesting that there are a significant number of locations with low $\overline{f}_c$, but $L_{50} \sim 100$ km over land that simply do not occur over oceans, and this helps to lower the correlation between L_{50} and $\overline{f}_c$ over land. These occur over arid regions where much of the cloud cover is made up of infrequent but extensive midlevel cloud sheets rather than small cumulus clouds.

Figure 11 shows that the power-law scaling exponent β has some dependency on the mean cloud cover $\overline{f}_c$, especially over ocean. For all locations, $\beta < 2$ indicating that the size distribution is weighted toward large clouds, but there are a number of locations and seasons where β approaches a value of 2. These regions where $\beta \approx 2$, however, are not those with the *lowest* cloud cover, but they do tend to be those with low L_{50}. In fact, β variability explains a significant fraction of the variance in L_{50} (see Fig. 12), as expected for a single power-law scaling for L extending from a few hundred meters to scales exceeding 1000 km. However, a fraction of the geographical variability in L_{50} is caused not by differences in the scaling exponent but by the location of the scale break [i.e., the value of L_* in Eq. (9)]. In other words, the scale break observed at approximately 1500–2000 km in the globally aggregated size distribution (Fig. 2), occurs at smaller scales in some regions, particularly (but not exclusively) those regions with low cloud cover. That said, seasonal/regional values of L_* are almost everywhere larger than 750 km, with median values of L_* being 1900 km over ocean and 1150 km over land. So, although L_{50} can be as low as 10 km in some regions, these regions still have cloud size distributions

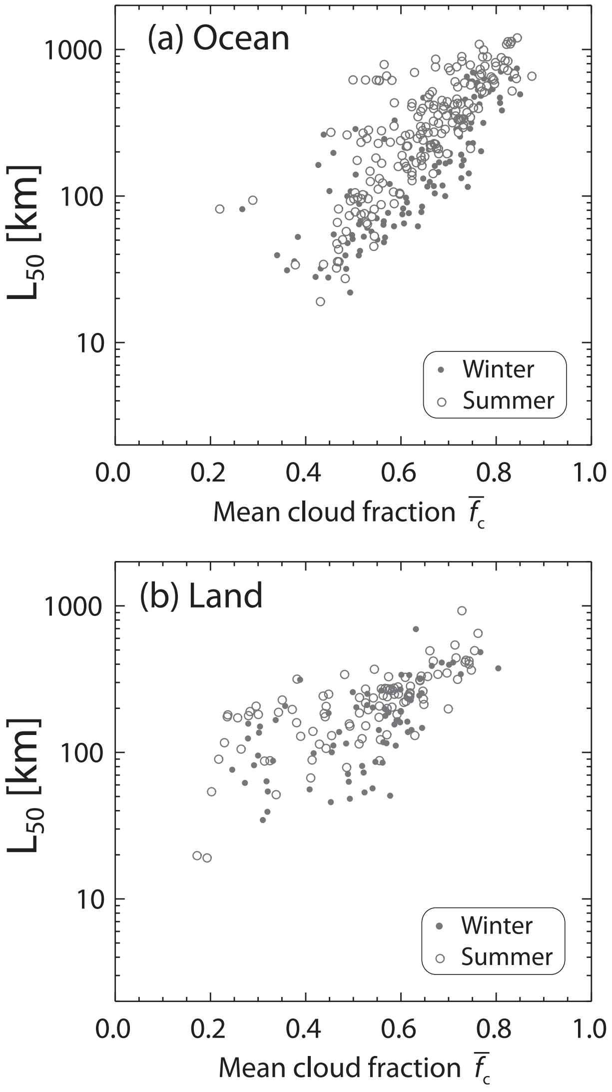

FIG. 10. Characteristic cloud chord length L_{50} as a function of the seasonal mean cloud fraction for the 20° × 20° regions shown in Fig. 8. The data are shown separately for (a) ocean and (b) land. For each, the results are broken down into the winter and summer hemisphere.

that observe power-law scaling out to many hundreds of kilometers.

d. On the scale break at approximately 2000 km

The statistically significant scale break observed in both the observations and global model contradicts the notion of a single scaling out to the planetary scale, and it is important to point out that the results in Lovejoy et al. (2001) required an extrapolation (albeit a theoretically sound one) and did not actually robustly sample clouds larger than 1500–2500 km. Figure 3 demonstrates that the scale break occurs at a slightly larger scale during Northern Hemisphere (NH) winter ($L_* \sim 2400$ km for JFM) compared to that for the NH summer ($L_* \sim 1750$ km during JJA). Additional analysis of the UM output (not shown) indicates that the scale break is almost identical in both the zonal and meridional directions. Seasonal maps (e.g., Fig. 9) indicate that the larger clouds in JFM stem from large clouds over the summertime Southern Ocean that are not matched with equally large clouds over the NH in boreal summer. Since the largest clouds are typically found over the oceans (section 3c), the seasonal differences in global cloud size distributions are likely explained by the hemispheric differences in the area of the midlatitudes covered with ocean.

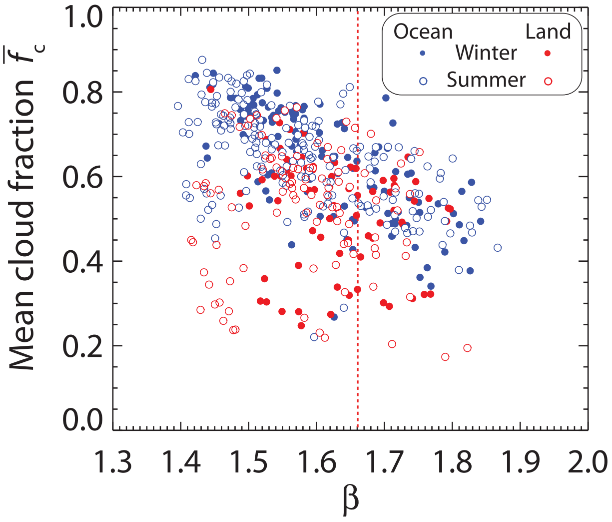

FIG. 11. Scaling exponent β of the power-law size distribution for the 20° × 20° regions shown in Fig. 8, plotted against the mean cloud cover. Data for winter and summer land and ocean are plotted separately using the same color scheme as in Fig. 10. The vertical line shows the exponent $\beta = 1.66$ derived from the aggregate size distribution from the entire MODIS dataset.

But why is there a robust scale break in the cloud horizontal size distribution at all? The characteristic scale L_* defining the scale break maximizes in midlatitudes (where median $L_* \approx 2000$ km) and is somewhat lower (median $L_* \approx 1500$ km) in the subtropics and tropics. According to Eq. (9), where $L = L_*$, the number of clouds is already a factor of 3 lower than expected from the single power-law scaling, and so the location where the distribution begins to diverge from a power law is somewhat smaller than L_*. In midlatitudes, the characteristic length scale governing the size of midlatitude cyclones is the Rossby radius, which has a typical length scale of ~1000 km. Thus, it is reasonable to hypothesize that the Rossby radius, by controlling the characteristic size of midlatitude weather systems, also controls the scale break in the cloud size distribution. This does not explain the scale breaks

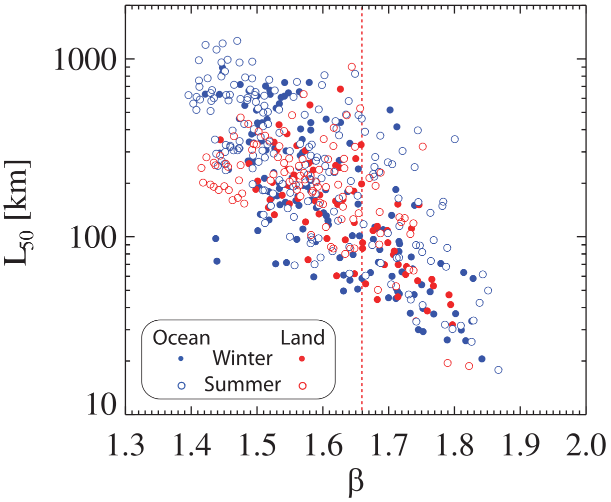

FIG. 12. Characteristic cloud scale L_{50} as a function of the scaling exponent β of the power-law size distribution for the 20° × 20° regions shown in Fig. 8. Data for winter–summer and land–ocean are plotted separately using the same color scheme as in Fig. 10. The red vertical line shows the exponent $\beta = 1.66$ derived from the aggregate size distribution from the entire MODIS dataset.

observed in the tropics, however, where the conventional Rossby radius becomes large and yet the scale break is actually smaller than in midlatitudes. There are other possible factors that limit the maximum cloud size (e.g., the distribution of landmasses, orography, and convective organization). Idealized experiments with aquaplanet GCMs may shed some light on the factors controlling the maximum horizontal cloud scale.

4. A simple physical model

To explore the physical causes for the observed power-law scaling of observed cloud chord lengths, and to explore some potential sampling artifacts, we use the simple bounded cascade fractal model of (Marshak et al. 1994). The bounded cascade model has been shown to faithfully replicate some of the key statistical and scaling properties of observed geophysical systems including those of clouds and the thermodynamic fields that control them (e.g., Davis et al. 1996; Cahalan et al. 1994; Marshak et al. 1997), since (in contrast to the scale-independent multiplicative cascade model) it can reproduce the Kolmogorov-type (“5/3”) scaling that observations show is consistent with the observed scaling of tropospheric moisture (Kahn and Teixeira 2009; Kahn et al. 2011) and other thermodynamic and dynamic fields (e.g., Nastrom and Gage 1985; Lovejoy et al. 2010). In regions of extensive marine stratocumulus, cloud variables such as cloud liquid water content (Davis et al. 1999), liquid water path (Wood and Taylor 2001; Wood and Hartmann 2006), and surface downwelling shortwave radiation (Comstock et al. 2005) also display exponents that are relatively close to the Kolmogorov scaling, at least over scales up to several tens of kilometers. This is the typical outer scale of the mesoscale organization inherent in marine stratocumulus sheets (Wood and Hartmann 2006).

To generate a multiplicative cascade field, one begins with a uniform field in one dimension. Then, the field is bisected and some fraction W_1 of one-half is transferred to the other half (the gaining half being chosen at random). Then, each half is itself bisected, and a fraction W_2 transferred from one-half to the other half, deciding again at random which half will be the recipient. This is shown schematically in Fig. 13. Scale-independent weights $W =$ constant lead to the simple multiplicative cascade. We choose to use the more realistic bounded cascade whereby $W_i = (1 - 2p)/2^{H(i-1)}$, with H $(0 < H < \infty)$ determining the scaling, and p $(0 < p < 1/2)$ controlling the field intermittency. The variance falls off more rapidly at smaller scales when H is large, and fields become more intermittent (or “bursty”) as p approaches 0. A value of $H = 1/3$ is consistent with Kolmogorov scaling, while we find that values of $p \sim 0.3$ give intermittency scaling consistent with that of cloud liquid water (Davis et al. 1996). For the bounded cascade model, we choose values of p from 0.2 to 0.4, which lead to the appropriate intermittency behavior.

We simulate one-dimensional spatial series of cloud occurrence by assuming that our simulated parent field is indicative of the atmospheric water column. When this value exceeds some threshold, we assume that there is cloud, and then proceed to characterize the cloud chord length distribution using the method discussion in section 2a above. We simulate parent fields that are 32 768 pixels in length, where a pixel is assumed to be 1 km in scale (although this is arbitrary). The threshold is chosen to produce a cloud fraction of 0.5 for each series realization, but experimentation with the model shows that the results are relatively insensitive to the precise choice of cloud fraction.

a. Model cloud chord length distributions

The model produces parent fields that generate cloud chord length distributions that are well represented by power laws, consistent with the observations. Figure 14 shows the relationship between the exponent of the model cloud length distribution $n(L)$ as a function of the scaling parameter H. Experimentation with the model shows that H is the key determinant of the exponent β in the model, and other factors (such as the intermittency and cloud fraction) are less important. Thus, in the model at least, there is a near-unique relationship between the scaling of the fundamental underlying

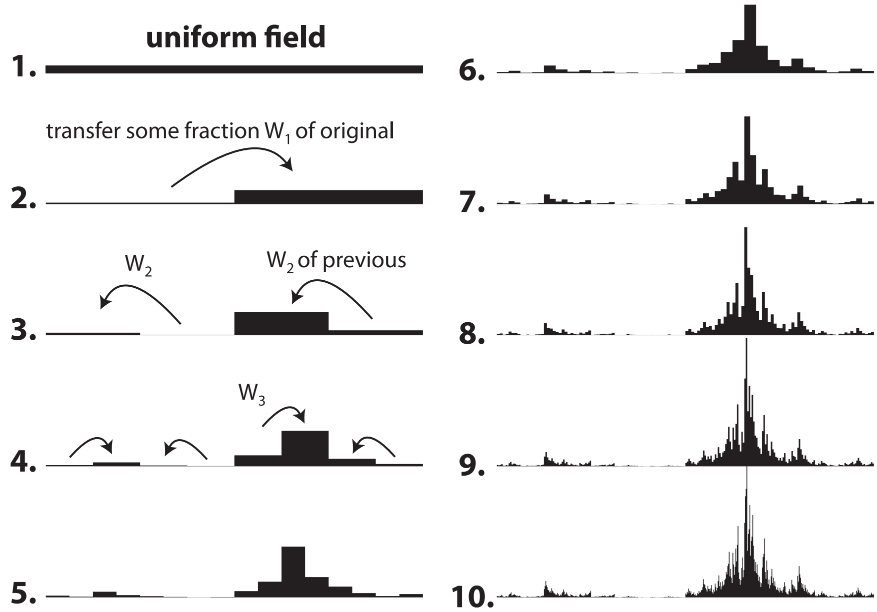

FIG. 13. Schematic of construction of one-dimensional fields from the bounded cascade model. Begin with a uniform field. Transfer some fraction W_1 from one-half to the other (with direction chosen at random). Then bisect each half and repeat process, but transferring a different fraction W_2 of each half. Repeat process with fractions W_i (called weights) until the resolution of data (pixel scale) is reached. For the bounded cascade, the weights $W_i = (1 - 2p)/2^{h(i-1)}$, where H ($0 < 0\ H < \infty$) determines the scaling, and p ($0 < p < 1/2$) controls the field intermittency, are the model parameters. In this particular example, which is intended to be illustrative, $H = 0.3$ and $p = 0.1$.

thermodynamic field and the exponent of the cloud size distribution. The observed exponent ($\beta \approx 1.66$ globally) is consistent with a scaling of the parent field in the range $H \approx 0.2$–0.35 (Fig. 14). Since $2H + 1$ is the exponent b of the energy spectrum power law for the parent field (see, e.g., Davis et al. 1996), these H values are consistent with observations of scaling in the thermodynamic fields as discussed at the start of this section. Thus, we can view the observed cloud size scaling exponent of $\beta \approx 1.7$ as consistent with controlling thermodynamic fields that obey Kolmogorov, or near-Kolmogorov scaling. But note the inverse dependence of β on H, indicating that smooth (large H) controlling thermodynamic fields (i.e., those with much energy at large scales) have a greater proportion of large clouds than highly variable fields. Only for $H \approx 0.3$ does $\beta \approx 2H + 1$ for the model (see Fig. 14).

Since almost everywhere the cloud size $n(L)$ demonstrates no scale break in the range $1 < L < 1000$ km (e.g., Fig. 2), based on the bounded cascade model results we might expect there not to be one in the underlying thermodynamic fields. It is interesting that the aircraft observations of Nastrom and Gage (1985) show a clear-scale break in the potential temperature and wind fields at horizontal scales $L \approx 300$–400 km. The scale break in temperature has been confirmed with global data from the Atmospheric Infrared Sounder (AIRS), but the AIRS instrument also demonstrates the absence of a clear scale break in the tropospheric specific humidity (Kahn and Teixeira 2009). Cloud fields are essentially slaved to the relative humidity (RH) rather than to specific humidity per se. But there is evidence that on the mesoscale, RH variability is more strongly tied to humidity variability than to temperature variability (Price and Wood 2002), also inferable from Fig. 5 in (Kahn and Teixeira 2009), and so we would therefore expect the cloud size distribution scaling to be more closely tied to the behavior of specific humidity rather than temperature (this also justifies a posteriori our model assumption). Furthermore, temperature fluctuations are likely to be damped by gravity waves through their effect on buoyancy. Scale breaks at a few hundred kilometers in the temperature and wind fields therefore, do not necessarily preclude single power-law scaling in cloud fields over a wider range of scales. Thus, the recent arguments of Lovejoy et al. (2010), which suggest that the Nastrom and Gage (1985) scale breaks may be artifacts of the commercial aircraft sampling strategy, may not be needed to understand cloud scaling over the range $0.1 < L < 2000$ km as observed in this study. However,

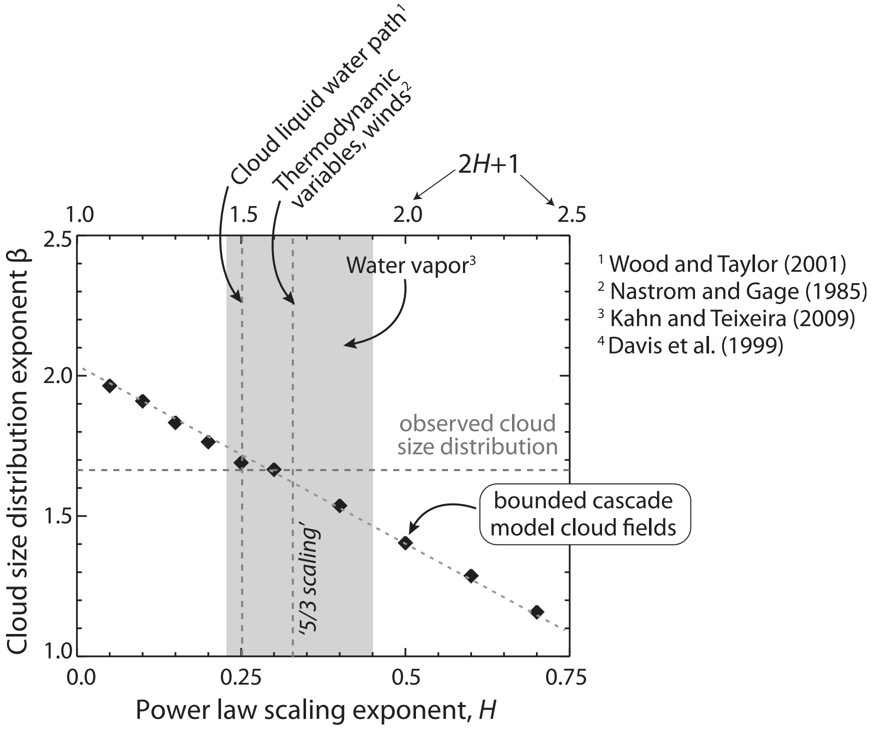

FIG. 14. Cloud chord length distribution power-law exponent β for one-dimensional discrete synthetic fields plotted as a function of the scaling exponent H of the parent moisture field used to create the cloud field. Each point represents a different value of the scaling parameter H and is created from 100 realizations of the bounded cascade model each with 32 768 pixels. The top axis shows $2H + 1$, which is the approximate power spectral exponent for the underlying field (Marshak et al. 1994). The gray shaded area represents the range of scaling parameters deduced from various thermodynamic and dynamic variables in the troposphere (see references). The observed clouds size distribution has an exponent of $\beta = 1.66$ globally (Fig. 2).

we still do not have a good understanding of the physics behind atmospheric moisture scaling.

b. *Effects of limited domain size on size distributions*

Using the bounded cascade model cloud fields described in the previous section we can investigate some issues that have been raised in the literature regarding the effects of sensor resolution and image size on the derived cloud size distributions. Specifically, Koren et al. (2008) use high-resolution visible satellite data from a scene containing small cumulus clouds, and degrade the resolution by coarse-graining to give larger pixels. They then apply the same visible radiance threshold to the lower-resolution pixels and derive the cloud area distribution. In doing so, the power-law exponent of the scaling decreases and the cloud area distribution shifts to larger sizes. It is natural to conclude that scaling exponents are sensitive to sensor resolution. We can test this hypothesis using the bounded cascade model fields. To do this, we coarse-grain our underlying parent fields before thresholding to determine the presence or absence of cloud. This is exactly the same process that Koren et al. (2008) applies to the satellite image data, except that we choose to use one-dimensional fields for simplicity.

Figure 15 shows the effect of coarse-graining (degrading sensor resolution) on the cloud chord length distributions from the bounded cascade model. As in Koren et al. (2008) we find that in general, increasing the pixel size can lead to a reduction in the slope of the cloud size distribution. However, we note that this tends to occur more readily when the domain size is small (cf. different domain sizes in Fig. 15a). When the domain size is sufficiently large that the ratio of domain to pixel scale is ~1000 or more, there is little or no change in the slope of the size distribution as the resolution degrades. Although not quantitatively comparable to the area distribution analysis of Koren et al. (2008), we can understand this behavior in the following way: as the pixel resolution is degraded, single clouds tend to coagulate to form larger clouds at lower resolution. When there is only a small domain size, there is a tendency for the size distribution to increase the number of intermediate

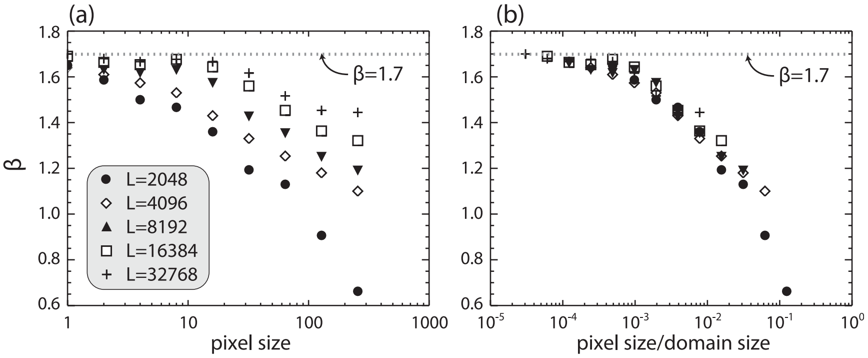

FIG. 15. Cloud chord length scaling exponent β from synthetic one-dimensional cloud fields created with the bounded cascade model, plotted against (a) the coarse-grained pixel size and (b) the ratio of the pixel size to the domain size L. For every synthetic field, $H = 0.25$ and $p = 0.2$, which gives a fundamental cloud chord scaling exponent of $\beta \approx 1.7$ (see Fig. 14). Results are shown for a variety of different series lengths (domain sizes) as indicated in the legend. The horizontal dotted line shows the exponent $\beta = 1.7$, which is close to the exponent for a pixel size of 1.

sized clouds at the expense of small clouds. However, if there is a sufficient domain size, there will also be a loss of these intermediate clouds to large clouds and a general cascade across the size distribution, which does not result in large changes to the exponent β. However, if the domain size is restrictive, this process is not allowed to happen naturally and clouds tend to pile up at scales close to the domain size, with a corresponding reduction in the exponent β. This seems somewhat counterintuitive, but one can visualize by analogy with the notion of a turbulent inertial subrange where energy cascading through the eddy scales does not lead to a pile up of energy at small scales.

The sensor degradation in the Koren et al. (2008) analysis was carried out on portions of Landsat scenes. The exact image (domain) size is not reported in the paper, but the largest clouds, even when the image was degraded, were only ~3 km in horizontal extent, presumably because the image was selected to contain primarily small clouds. It appears that only small sections of the entire 185-km-wide Landsat images were used since the actual full images (available online at http://www.landcover.org) contain a number of larger clouds that do not appear to be included in the analysis. Thus, it seems reasonable to suppose that the 36-km-wide image shown in (Koren et al. 2008, their Fig. 1) represents the effective domain size used in the analysis. In this event, then the 30-m native Landsat pixels would have a domain: pixel size ratio of 1/1200, but the pixels degraded to approximate MODIS scale (960 m) would have a pixel/domain size ratio of only ~1/40. As we can see from Fig. 15, size distributions derived from data with this range of pixel/domain size ratio would be subjected to considerable artificial distortion, which does not reflect the fundamental scaling parameters of the underlying field. Based on these results we would caution against drawing any conclusions regarding the physical significance of any observed scaling for distributions derived from data for which the ratio of the series length to the sampling resolution is significantly less than 10^3.

5. Discussion and conclusions

The primary result of this study is the clear emergence of power-law scaling in the near-global distribution of cloud sizes over at least four orders of magnitude of cloud horizontal scale (and >6 orders in cloud area). This might have been anticipated based on earlier studies that examined limited ranges of cloud size but found similar scaling exponents for these limited regimes. However, the use of ~1-km resolution data from MODIS to explore the cloud chord length distribution spanning almost 4 decades of scale (1–8000 km) allows a more complete examination than has been possible before.

The characteristic cloud horizontal scale L_{50}, the cloud size at which both larger and smaller clouds contribute equally to the cloud cover, is on average ~200 km, but does have significant geographical variations (with L_{50} ranging from a few kilometers to over 500 km). The large characteristic cloud size is a consequence of a scaling exponent β that is less than 2, which essentially means that L_{50} is governed by clouds close to the maximum size permitted than by the details of the smallest clouds. This result is broadly consistent with earlier studies showing that most of the spatial variance in cloud fields occurs on scales larger than a few tens of kilometers (Seze and Rossow 1991; Rossow et al. 2002).

We find that the cloud chord length scaling exponent β varies geographically, and variations in β can explain a large fraction of the variance in L_{50}, despite the fact that geographical variations in β are relatively modest (the 5th and 95th percentiles of β are 1.6 and 2.0, respectively). In regions dominated by small cumulus clouds (e.g., the tropical trades, and over some land regions in summer away from unstable regions), $\beta \approx 2$, which is consistent with exponents for small cumulus measured using very high-resolution satellite imagery (Benner and Curry 1998; Zhao and Di Girolamo 2007). In these regions, small clouds play a significant role in determining the cloud cover, but it should be stressed that even here larger clouds still contribute significantly to cloud cover and particularly solar reflectance (hence, L_{50} is typically at least 10 km for most of the trade wind regions). At the other extreme, summertime midlatitude ocean regions are characterized by smaller $\beta \approx 1.4-1.6$. Even these relatively small changes in β have a profound impact on the characteristic cloud size L_{50} because of the proximity to $\beta = 2$. The preference for β values of ≈ 2 appears to ensure that the earth experiences the widest possible variety (seasonal and geographical) of characteristic cloud sizes. It is perhaps for this reason that clouds continue to fascinate and challenge us.

There are some significant implications of our findings. A number of observational studies used to estimate aerosol indirect effects rely on correlations between cloud microphysical properties and aerosol properties derived from neighboring clear-sky regions (e.g., Quaas et al. 2008). It is questionable how representative aerosol retrievals will be of the neighboring cloudy airmasses for clouds that are typically a few hundred kilometers in scale. We do not explore this issue further in this study, but suggest that the representativeness issue is in need of exploration. In addition, over much of the globe, clouds larger than typical numerical weather prediction and even climate model grid boxes tend to constitute the majority of the cloud cover. This makes one wonder about whether the target for subgrid cloud parameterization scheme development should be the correct distribution of condensate as opposed to better prediction of cloud fractional coverage.

Acknowledgments. The authors wish to thank the staff of the Meteorological Research Flight and the C-130 aircrew and ground crew for their dedication to collecting the data presented in this study. MODIS data were obtained from the excellent NASA Level-1 and Atmosphere Archive and Distribution System (LAADS). We thank Marc Michelsen for his contributions to data aquisition and processing. We also thank Brian Kahn, Andrew Gettelman, Tim Garrett, Chris Bretherton, and Marcia Baker for suggestions that helped strengthen the manuscript.

REFERENCES

Ackerman, S. A., K. I. Strabala, W. P. Menzel, R. A. Frey, C. C. Moeller, and L. E. Gumley, 1998: Discriminating clear sky from clouds with MODIS. *J. Geophys. Res.,* **103** (D24), 32 141–32 157.

Albrecht, B. A., M. P. Jensen, and W. J. Syrett, 1995: Marine boundary layer structure and fractional cloudiness. *J. Geophys. Res.,* **100** (D7), 14 209–14 222.

Benner, T. C., and J. A. Curry, 1998: Characteristics of small tropical cumulus clouds and their impact on the environment. *J. Geophys. Res.,* **103** (D22), 28 753–28 767.

Bretherton, C. S., and M. C. Wyant, 1997: Moisture transport, lower-tropospheric stability, and decoupling of cloud-topped boundary layers. *J. Atmos. Sci.,* **54,** 148–167.

Cahalan, R. F., W. Ridgway, W. J. Wiscombe, S. Gollmer, and Harshvardhan, 1994: Independent pixel and Monte Carlo estimates of stratocumulus albedo. *J. Atmos. Sci.,* **51,** 3776–3790.

Comstock, K., C. S. Bretherton, and S. Yuter, 2005: Mesoscale variability and drizzle in Southeast Pacific stratocumulus. *J. Atmos. Sci.,* **62,** 3792–3807.

Cullen, M. J. P., T. Davies, M. Mawson, J. James, S. Coulter, and A. Malcolm, 1997: An overview of numerical methods for the next generation UK NWP and climate model. *Numerical Methods in Atmospheric and Ocean Modelling: The Andre J. Robert Memorial Volume,* C. A. Lin, R. Laprise, and H. Ritchie, Eds., Canadian Meteorological and Oceanographic Society, 425–444.

Davies, T., M. J. P. Cullen, A. J. Malcolm, M. H. Mawson, A. Staniforth, A. A. White, and N. Wood, 2005: A new dynamical core for the Met Office's global and regional modelling of the atmosphere. *Quart. J. Roy. Meteor. Soc.,* **131,** 1759–1782.

Davis, A., A. Marshak, W. Wiscombe, and R. Cahahlan, 1996: Scale invariance of liquid water distributions in marine stratocumulus. Part I: Spectral properties and strationarity issues. *J. Atmos. Sci.,* **53,** 1538–1558.

——, ——, H. Gerber, and W. J. Wiscombe, 1999: Horizontal structure of marine boundary layer clouds from cm to km scales. *J. Geophys. Res.,* **104,** 6123–6144.

Essery, R. L. H., M. J. Best, R. A. Betts, P. M. Cox, and C. M. Taylor, 2003: Explicit representation of subgrid heterogeneity in a GCM land surface scheme. *J. Hydrometeor.,* **4,** 530–543.

Field, P. R., and G. Shutts, 2009: Properties of normalised rain-rate distributions in the tropical Pacific. *Quart. J. Roy. Meteor. Soc.,* **135,** 175–186.

Gregory, D., and P. Rowntree, 1990: A mass flux convection scheme with representation of cloud ensemble characteristics and stability-dependent closure. *Mon. Wea. Rev.,* **118,** 1483–1506.

Kahn, B., and J. Teixeira, 2009: A global climatology of temperature and water vapor variance scaling from the atmospheric infrared sounder. *J. Climate,* **22,** 5558–5576.

——, and Coauthors, 2011: Temperature and water vapor variance scaling in global models: Comparisons to satellite and aircraft data. *J. Atmos. Sci.,* in press.

King, M. D., and Harshvardhan, 1986: Comparative accuracy of selected multiple scattering approximations. *J. Atmos. Sci.,* **43,** 784–801.

Klein, S. A., and D. L. Hartmann, 1993: The seasonal cycle of low stratiform clouds. *J. Climate,* **6,** 1588–1606.

Knollenberg, R. G., 1970: The optical array: An alternative to scattering or extinction for airborne particle size determination. *J. Appl. Meteor.,* **9,** 86–103.

Koren, I., L. Oreopoulos, G. Feingold, L. Remer, and O. Altaraz, 2008: How small is a small cloud? *Atmos. Chem. Phys.,* **8,** 3855–3864.

Lock, A. P., A. Brown, M. Bush, G. Martin, and R. Smith, 2000: A new boundary layer mixing scheme. Part I: Scheme description and single-column model tests. *Mon. Wea. Rev.,* **128,** 3187–3199.

Lovejoy, S. D., 1982: Area-perimeter relation for rain and cloud areas. *Science,* **216,** 185–187.

——, and D. Schertzer, 2006: Multifractals, cloud radiances and rain. *J. Hydrol.,* **322,** 58–88.

——, ——, and J. D. Stanway, 2001: Direct evidence of multifractal atmospheric cascades from planetary scales down to 1 km. *Phys. Rev. Lett.,* **86,** 5200–5203.

——, A. Tuck, and D. Schertzer, 2010: Horizontal cascade structure of atmospheric fields determined from aircraft data. *J. Geophys. Res.,* **115,** D13105, doi:10.1029/JD013353.

Machado, L., and W. B. Rossow, 1993: Structural characteristics and radiative properties of tropical cloud clusters. *Mon. Wea. Rev.,* **121,** 3234–3260.

——, T. M. Desbois, and J.-P. Duvel, 1992: Structural characteristics of deep convective systems over tropical Africa and the Atlantic Ocean. *Mon. Wea. Rev.,* **120,** 392–406.

Marshak, A., A. Davis, R. Cahalan, and W. J. Wiscombe, 1994: Bounded cascade models as non-stationary multifractals. *Phys. Rev. E Stat. Phys. Plasmas Fluids Relat. Interdiscip. Topics,* **49,** 55–79.

——, ——, W. Wiscombe, and R. Cahalan, 1997: Scale invariance in liquid water distributions in marine stratocumulus. Part II: Multifractal properties and intermittency issues. *J. Atmos. Sci.,* **54,** 1423–1444.

Nastrom, G., and K. Gage, 1985: A climatology of atmospheric wavenumber spectra of wind and temperature observed by commercial aircraft. *J. Atmos. Sci.,* **42,** 950–960.

Neggers, R., H. Jonker, and A. Siebesma, 2003: Size statistics of cumulus cloud populations in large-eddy simulations. *J. Atmos. Sci.,* **60,** 1060–1074.

Peters, O., J. D. Neelin, and S. W. Nesbitt, 2009: Mesoscale convective systems and crtical clusters. *J. Atmos. Sci.,* **66,** 2913–2924.

Plank, V. G., 1969: The size distribution of cumulus clouds in representative Florida populations. *J. Appl. Meteor.,* **8,** 46–67.

Platnick, S., M. D. King, S. A. Ackerman, W. P. Menzel, B. A. Baum, J. C. Riedi, and R. A. Frey, 2003: The MODIS cloud products: Algorithms and examples from Terra. *IEEE Trans. Geosci. Remote Sens.,* **41** (2), 459–473.

Price, J. D., and R. Wood, 2002: Comparison of probability density functions for total specific humidity and saturation deficity humidity, and consequences for cloud parameterization. *Quart. J. Roy. Meteor. Soc.,* **128,** 2059–2072.

Quaas, J., O. Boucher, N. Bellouin, and S. Kinne, 2008: Satellite-based estimate of the direct and indirect aerosol climate forcing. *J. Geophys. Res.,* **113,** D05204, doi:10.1029/2007JD008962.

Rodts, S. M. A., P. G. Duynkerke, and H. J. J. Jonker, 2003: Size distributions and dynamical properties of shallow cumulus clouds from aircraft observations and satellite data. *J. Atmos. Sci.,* **60,** 1895–1912.

Rossow, W. B., C. Delo, and B. Cairns, 2002: Implications of the observed mesoscale variations of clouds for earth's radiation budget. *J. Climate,* **15,** 557–585.

Seze, G., and W. Rossow, 1991: Effects of satellite data resolution on measuring the space-time variations of surfaces and clouds. *Int. J. Remote Sens.,* **12,** 921–952.

Smith, R. N. B., 1990: A scheme for predicting layer clouds and their water content in a general circulation model. *Quart. J. Roy. Meteor. Soc.,* **116,** 435–460.

Welch, R. M., K. S. Kuo, B. A. Wielicki, S. K. Sengupta, and L. Parker, 1988: Marine stratocumulus cloud fields off the coast of southern California observed using Landsat imagery. Part I: Structural characteristics. *J. Appl. Meteor.,* **27,** 341–362.

Wilcox, E. M., and V. Ramanathan, 2001: Scale dependence of the thermodynamic forcing of tropical monsoon clouds: Results from TRMM observations. *J. Climate,* **14,** 1511–1524.

Wilson, D. R., and S. P. Ballard, 1999: A microphysically based precipitation scheme for the UK Meteorological Office unified model. *Quart. J. Roy. Meteor. Soc.,* **125,** 1607–1636.

Wood, R., and P. R. Field, 2000: Relationships between total water, condensed water, and cloud fraction in stratiform clouds examined using aircraft data. *J. Atmos. Sci.,* **57,** 1888–1905.

——, and J. P. Taylor, 2001: Liquid water path variability in unbroken marine stratocumulus. *Quart. J. Roy. Meteor. Soc.,* **127,** 2635–2662.

——, and C. S. Bretherton, 2004: Boundary layer depth, entrainment, and decoupling in the cloud-capped subtropical and tropical marine boundary layer. *J. Climate,* **17,** 3576–3588.

——, and D. L. Hartmann, 2006: Spatial variability of liquid water path in marine boundary layer clouds: The importance of mesoscale cellular convection. *J. Climate,* **19,** 1748–1764.

Zhao, G., and L. Di Girolamo, 2007: Statistics on the macrophysical properties of trade wind cumuli over the tropical western Atlantic. *J. Geophys. Res.,* **112,** D10204, doi:10.1029/2006JD007371.